JACS
JOURNAL OF THE AMERICAN CHEMICAL SOCIETY
pubs.acs.org/JACS
Article

Tailoring Charge Separation at Meticulously Engineered Conjugated Polymer/Perovskite Quantum Dot Interface for Photocatalyzing Atom Transfer Radical Polymerization

Shuang Liang, Sheng He, Mingyue Zhang, Yan Yan, Tao Jin, Tianquan Lian, and Zhiqun Lin*

Cite This: J. Am. Chem. Soc. 2022, 144, 12901−12914

ABSTRACT: In stark contrast to conventional organic ligand-capped counterparts, the ability to create stable metal halide perovskite nanocrystals strongly tethered with conjugated polymers (CPs) represents an important endeavor toward tailoring charge carrier dynamics at their interface that critically underpins applications of this unique class of all semiconducting, organic−inorganic nanomaterials for optoelectronics. This, however, has yet to be largely explored. Herein, we report, for the first time, the unraveling of efficient charge separation at judiciously designed CP/perovskite quantum dot (QD) interface for photoinduced atom transfer radical polymerization (p-ATRP). Such scrutiny is rendered by *in situ* crafting an array of monodisperse, highly stable, CP-ligated perovskite QDs with precisely controlled dimensions of each constituent via capitalizing on unimolecular, amphiphilic starlike block copolymers as nanoreactors. The intimate and permanent surface tethering of CPs imparts remarkable thermal, photo, and polar solvent stabilities of CP-ligated perovskite QDs. More importantly, they manifest efficient interfacial charge separation with a profound dependence on the length of ligated CPs and the size of perovskite QDs. The outstanding structural stabilities and charge separation characteristic enable CP-ligated perovskite QDs as robust photocatalysts for p-ATRP of a wide selection of monomers with stable and controllable reaction kinetics, also depending crucially on the length of CPs and the size of perovskite QDs. In principle, an exciting variety of CP-ligated, uniform perovskite QDs with virtually unlimited material choice of both markedly improved stabilities and tunable electronic band alignments can be readily accessed by exploiting the amphiphilic starlike block copolymer nanoreactor strategy for use in photodetectors, sensors, and LEDs, among other areas.

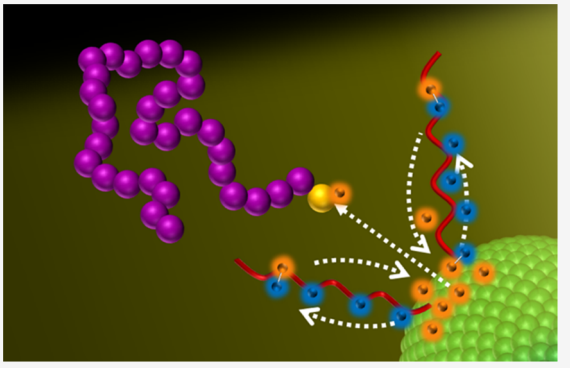

INTRODUCTION

The past several years has witnessed rapid advances in synthesis and utilities of metal halide perovskite nanocrystals (hereafter referred to as quantum dots (QDs)) due to a set of appealing attributes, including size- and composition-dependent electronic band gap,[1] high quantum yield (QY),[2] and narrow emission full width at half-maximum (FWHM),[1] improved structural and phase stability over thin-film counterparts owing to their surface capping with organic ligands,[3] ambient solution processability,[4] etc. They find applications in solar cells, light-emitting diodes (LEDs), sensors, and photocatalysis. In the latter context, perovskite QDs have been exploited for photocatalytic organic synthesis,[5] water splitting,[6] and carbon dioxide reduction[7] because of tunable band gap, low cost, and ease of synthesis of perovskite QDs, and their high reaction kinetics toward photocatalytic organic synthesis.[5] Notably, photoinduced atom transfer radical polymerization (p-ATRP), one form of robust living polymerization techniques, involves the use of photocatalysts (e.g., carbon dots,[8] conventional semiconducting QDs,[9] or up-converting nanoparticles[10]) to produce functional polymers with precise sequence and molecular weight (MW), narrow MW distribution, and well-defined architectures under mild conditions.[11] Surprisingly, despite advantageous characteristics noted above, perovskite QDs have yet to be explored in p-ATRP.

Despite small molecular organic ligands (often insulating) generally employed to stabilize the surface and passivate surface defects on perovskite QDs,[4] their long-term use in optoelectronic materials and devices is greatly plagued by their intrinsic instability toward external stimuli (humidity, heat, UV irradiation, and polar solvents) due to the ionic crystal nature.[12] Moreover, to promote charge carrier transfer among QDs for optoelectronics, recent research introduced conjugated small molecules with high electrical conductivity as

Received: May 1, 2022
Published: July 11, 2022

https://doi.org/10.1021/jacs.2c04680
J. Am. Chem. Soc. 2022, 144, 12901−12914

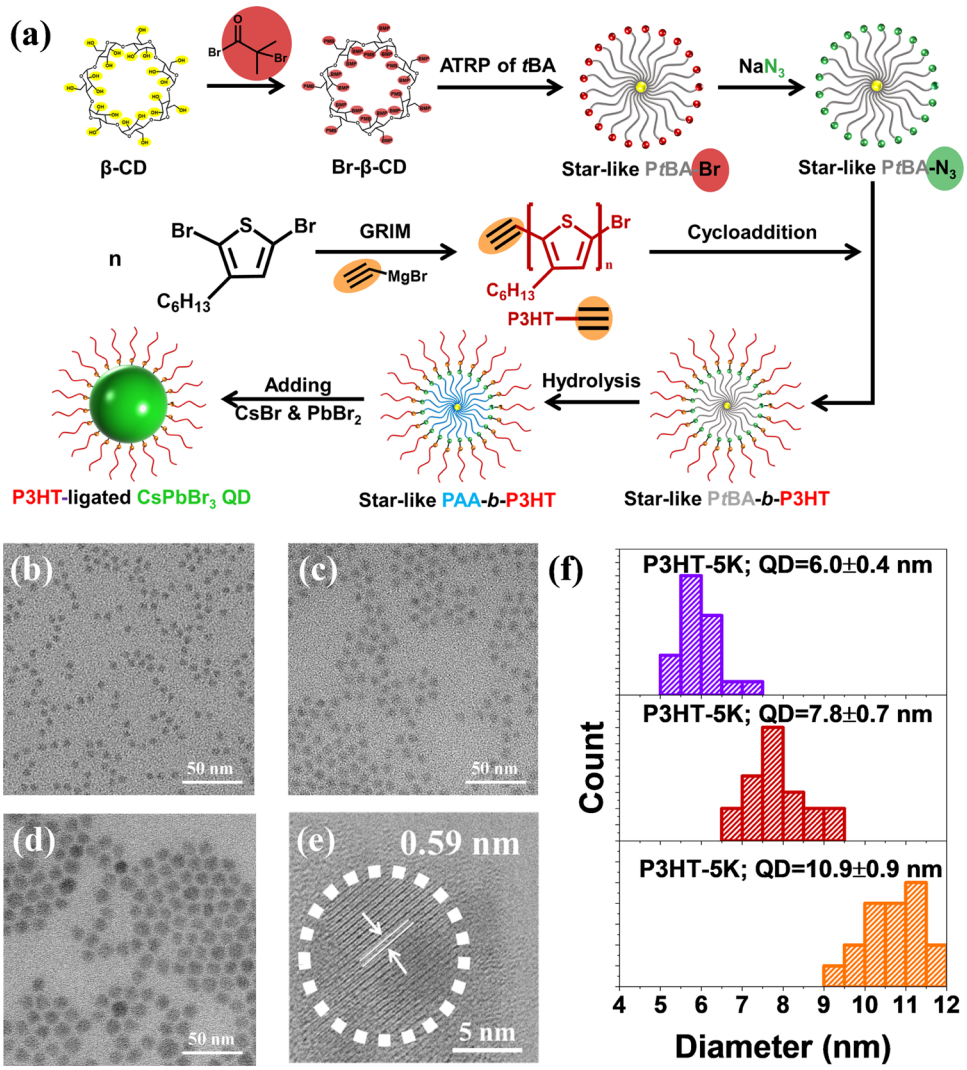

Figure 1. Synthesis of P3HT-ligated $CsPbBr_3$ QDs. (a) Schematic representation of crafting $CsPbBr_3$ QD via capitalizing on starlike PAA-*b*-P3HT block copolymer as a nanoreactor. (b–d) TEM images of P3HT-ligated $CsPbBr_3$ QDs with diameters *D* of (b) 6.0 ± 0.4 nm, (c) 7.8 ± 0.7 nm, and (d) 10.9 ± 0.9 nm crafted using PAA-*b*-P3HT-1, PAA-*b*-P3HT-2, and PAA-*b*-P3HT-5 with the fixed length of P3HT chains as nanoreactors, respectively. (e) High-resolution TEM (HRTEM) image of a P3HT-ligated $CsPbBr_3$ QD (white cycle is a guide to the eye). (f) Statistics of size distribution of as-synthesized QDs.

ligands during colloidal synthesis of perovskite QDs[13,14] or via postsynthesis ligand exchange.[15] However, the former approach yields perovskite QDs with low size and morphology uniformity.[13,14] For the latter method, exchanging insulating hydrocarbon ligands with conjugated small molecules may result in damaging of QDs and incomplete substitution due to their liability to decomposition and competitive binding of two different ligands, respectively.[16] Nonetheless, these issues may limit the full potential of conjugated small-molecule-capped perovskite QDs for optoelectronics. In this context, due to both fundamental and practical importance, it is highly desirable to develop a viable route to placing conjugated molecules in permanent contact with perovskite QDs to achieve enhanced optoelectronic properties, while retaining good control over their size and morphology; this, however, remains challenging. Particularly, the ability to stably tether conjugated polymers on perovskite QDs, rather than conjugated small molecules,[17,18] expands the diversity of perovskite QDs accessible and the portfolio of photophysical properties.

Herein, we report, for the first time, the tailoring of charge separation at a series of meticulously engineered CP/perovskite QD interfaces with staggered type-II band alignment via precisely regulating the length of CPs as well as the size of perovskite QDs in CP-ligated, monodisperse perovskite QDs. The associated rapid charge separation kinetics in turn render their use as robust photocatalysts for effective p-ATRP of monomers of interest. Strikingly, the length of ligated CPs and the size of perovskite QDs are found to exert a profound influence on charge separation kinetics and p-ATRP. Specifically, poly(3-hexylthiophene) (P3HT) and $CsPbBr_3$ are chosen as model CP and perovskite QD, respectively. First, an array of P3HT-ligated, uniform $CsPbBr_3$ QDs with varied diameters and P3HT lengths are crafted by leveraging a gamut of unimolecular, amphiphilic starlike poly(acrylic acid)-*block*-poly(3-hexylthiophene) (denoted PAA-*b*-P3HT) block copolymers with tunable MWs of each block as nanoreactors. The inner hydrophilic coil-like PAA blocks of various MWs direct the growth of $CsPbBr_3$ QDs, thus dictating their diameters. On the other hand, the outer hydrophobic

https://doi.org/10.1021/jacs.2c04680
J. Am. Chem. Soc. 2022, 144, 12901−12914

conjugated P3HT blocks of different MWs function as surface ligands that are intimately and firmly tethered on the surface of $CsPbBr_3$ QD as a result of original covalent bonding between PAA and P3HT blocks in starlike PAA-*b*-P3HT. As a result, a host of P3HT-ligated uniform $CsPbBr_3$ QDs are formed, displaying a set of appealing stabilities against water, heat, light, and polar solvents, as well as yielding favorable staggered type-II band alignment between P3HT and $CsPbBr_3$ QD for efficient charge separation (only 0.31 versus 2.10 ns in the physical mixture of P3HT/$CsPbBr_3$ QD, representing a 7-fold decrease in intrinsic band-to-band photoluminescence lifetime). The remarkable stabilities in conjunction with efficient yet tailorable charge separation characteristic make P3HT-ligated $CsPbBr_3$ QDs effective photocatalysts for p-ATRP of a wide range of monomers with stable and controllable reaction kinetics. The ability to construct CP-ligated, monodisperse perovskite QDs with conveniently tuned dimensions of both constituents enabled by unimolecular starlike block copolymer strategy to scrutinize optical properties and charge carrier dynamics would underpin the advances and utilities of this unique class of nanomaterials in catalysis, optoelectronics, nanotechnology, and biotechnology, as it circumvents a set of issues associated with ligand dissociation, insulating small molecular ligand characteristic, nonuniform morphology, and phase segregation in copious past works on perovskite QDs.

RESULTS AND DISCUSSION

First, a set of amphiphilic starlike PAA-*b*-P3HT block copolymers with varied yet well-defined MW and narrow MW distribution of each block were synthesized via combining ATRP with click reaction. Figure 1 depicts the route to monodisperse, P3HT-ligated $CsPbBr_3$ QDs via capitalizing on starlike PAA-*b*-P3HT as nanoreactors (see the Experimental Section in the Supporting Information). Briefly, brominated *β*-cyclodextrin (denoted Br-*β*-CD) was first synthesized by the esterification of *β*-CD with 2-bromoisobutylbromide with nearly 100% conversion of the hydroxyl groups on *β*-CD into *ω*-bromide terminals, as confirmed by ^{1}H nuclear magnetic resonance (NMR) spectroscopy (Figure S1).[19] The subsequent use of Br-*β*-CD as macroinitiator for ATRP of *tert*-butyl acrylate (*t*BA) produced starlike poly(*tert*-butyl acrylate) (P*t*BA; ^{1}H NMR in Figure S2), followed by converting *ω*-bromide terminals to azide functionalities ($-N_3$) to yield azide-terminated starlike P*t*BA (denoted P*t*BA-N_3) via the S_N2 reaction (first row; Figure 1). On the other hand, ethynyl-terminated P3HT (denoted P3HT-≡, ^{1}H NMR in Figure S4) was synthesized by Grignard metathesis polymerization of 2,5-dibromo-3-hexylthiophene monomer using Ni-based metal complexes as catalyst, followed by alkyne functionalization via reacting with ethynylmagnesium bromide (second row; Figure 1). Afterward, P3HT-≡ was clicked onto starlike P*t*BA-N_3 via copper-catalyzed azide-alkyne cycloaddition reaction, yielding starlike P*t*BA-*b*-P3HT (^{1}H NMR; Figure S5). The hydrolysis of inner P*t*BA blocks into PAA blocks produced amphiphilic starlike PAA-*b*-P3HT composed of inner coil-like hydrophilic PAA blocks and outer rod-like hydrophobic P3HT blocks (third row; Figure 1) with a typical yield of 100−200 mg per batch.

Star-like PAA-*b*-P3HT was then used as a nanoreactor for *in situ* crafting P3HT-ligated, monodisperse $CsPbBr_3$ QD (first panel, third row; Figure 1). Typically, starlike PAA-*b*-P3HT block copolymers were first dissolved in DMF, a good solvent for inner PAA,[19] whereas it is a poor solvent for outer P3HT,[20] to form stable unimolecular micelles with fully expanded PAA chains and collapsed P3HT chains. Subsequently, perovskite precursors (CsBr and $PbBr_2$) were introduced into the solution under vigorous stirring (see the Experimental Section). CsBr and $PbBr_2$ were selectively partitioned in the compartment occupied by inner PAA blocks, driven by strong coordination between carboxylic groups (−COOH) of PAA blocks and metal ions of precursors (CsBr and $PbBr_2$), forming precursor-loaded starlike PAA-*b*-P3HT DMF solution. Finally, the solution was dropwise added into a mixture of toluene and chlorobenzene (volume ratio = 8:2) to rapidly yield P3HT-ligated $CsPbBr_3$ QDs. After washing with methyl acetate as a poor solvent and toluene as a good solvent three times, the resulting P3HT-ligated $CsPbBr_3$ QDs were dispersed in toluene to form a stable colloidal solution without precipitant.

Notably, $CsPbBr_3$ QDs are intimately and firmly ligated with P3HT chains due to the original covalent bonding between PAA and P3HT blocks. In other words, our nanoreactor strategy offers easy access to stable CP-ligated PQDs at a single-particle level that would otherwise be difficult to achieve. Consequently, P3HT-ligated $CsPbBr_3$ QDs with varied lengths of P3HT and diameters of QDs can be readily accessed by tuning the MWs of P3HT and PAA blocks via controlling the Grignard metathesis polymerization time of 2,5-dibromo-3-hexylthiophene monomers and ATRP time of *t*BA monomers, respectively.

Figure 1b−d shows representative transmittance electron microscopy (TEM) images of P3HT-ligated $CsPbBr_3$ QDs of different diameters templated by three respective starlike PAA-*b*-P3HT nanoreactors (i.e., PAA-*b*-P3HT-1, PAA-*b*-P3HT-2, and PAA-*b*-P3HT-5; Table 1). The average diameters *D* of

Table 1. Summary of MWs and PDIs of Starlike PAA-*b*-P3HT Block Copolymer Nanoreactors, and the Corresponding Dimension of P3HT-Ligated $CsPbBr_3$ QDs

samples	$M_{n,PAA}$[a] (g/mol)	$M_{n,P3HT}$[b] (g/mol)	PDI[c]	diameter of $CsPbBr_3$ QDs[d] (nm)
PAA-*b*-P3HT-1	4900	5000	1.13	6.0 ± 0.4
PAA-*b*-P3HT-2 (P3HT-5K)	6700	5000	1.10	7.8 ± 0.7
PAA-*b*-P3HT-3 (P3HT-10K)	6700	9800	1.12	8.0 ± 0.6
PAA-*b*-P3HT-4 (P3HT-15K)	6700	15,200	1.16	7.7 ± 0.7
PAA-*b*-P3HT-5	8900	5000	1.17	10.9 ± 0.9

[a] $M_{n,PAA}$ is the MW of single-arm PAA calculated by ^{1}H NMR spectra from the MW difference between single-arm P*t*BA (before hydrolysis) and PAA (after hydrolysis) following the below equation:

$$M_{n,PAA} = \frac{72.06}{128.17} \times M_{n,PtBA} = \frac{72.06}{128.17} \times \frac{A_b/9}{A_a/6} \times 128.17$$

where A_b and A_a are the integral areas of the methyl protons in the *tert*-butyl group of P*t*BA chain and at the *α*-end of P*t*BA chain in the ^{1}H NMR spectra, respectively, and 128.17 and 72.06 are the MWs of *t*BA monomer and AA repeat unit, respectively.

$CsPbBr_3$ QDs are 6.0 ± 0.4 nm (from PAA-*b*-P3HT-1, Figure 1b), 7.8 ± 0.7 nm (from PAA-*b*-P3HT-2, Figure 1c), and 10.9 ± 0.9 nm (from PAA-*b*-P3HT-5, Figure 1d), respectively, suggesting their high size uniformity (hereafter referred to as 6, 8, and 11 nm QDs). Notably, the MWs of outer P3HT blocks of the three nanoreactors are identical (Table 1), indicating that the diameter of $CsPbBr_3$ QDs is dictated by the MW (i.e.,

https://doi.org/10.1021/jacs.2c04680
J. Am. Chem. Soc. 2022, 144, 12901−12914

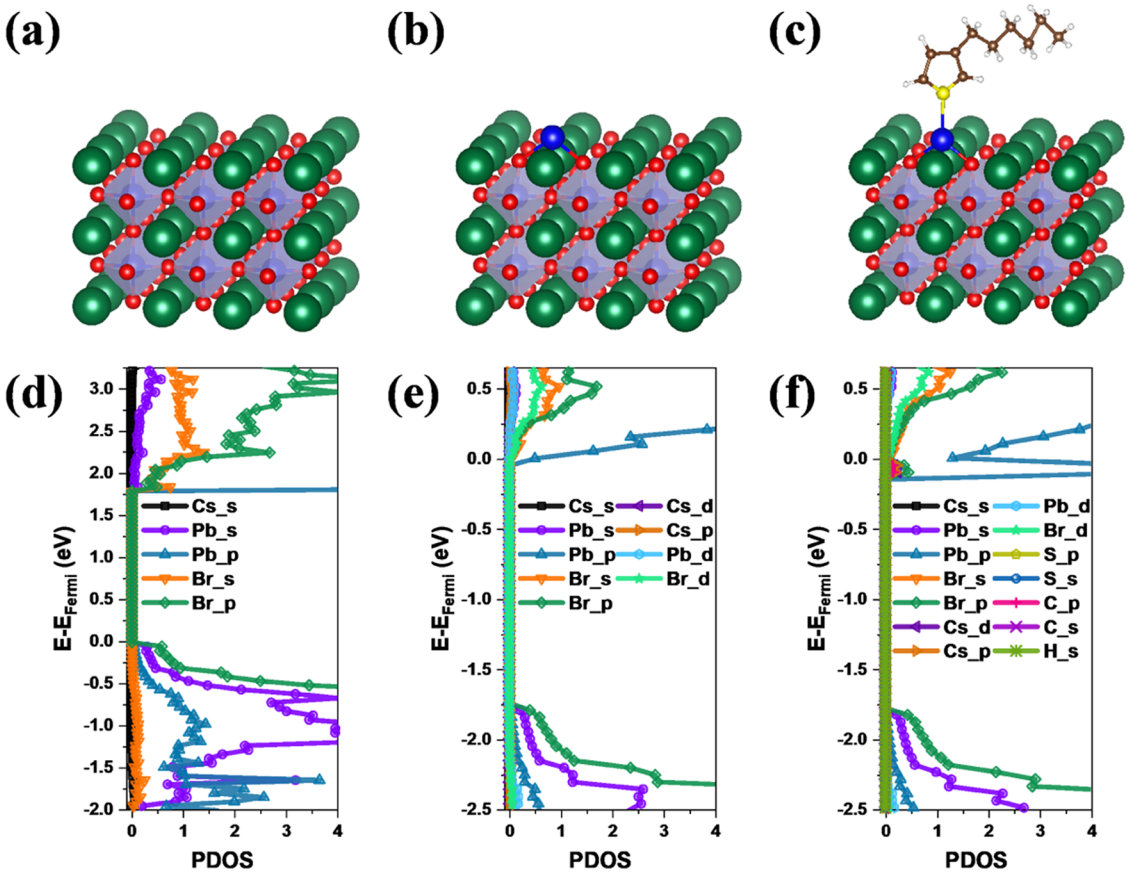

Figure 2. Molecular interaction between 3HT and $CsPbBr_3$ QD. Schematic diagram of part of the simulated slab of (a) bare $CsPbBr_3$, (b) $CsPbBr_3$ with Pb interstitials, and (c) 3HT-modified $CsPbBr_3$ with Pb interstitials. (d–f) Electronic projected density of states (pDOS) of (d) bare $CsPbBr_3$, (e) $CsPbBr_3$ with Pb interstitials, and (f) 3HT-modified $CsPbBr_3$ with Pb interstitials.

chain length) of inner PAA blocks as noted above. On the other hand, as shown in Figure S8, with the fixed MW of inner PAA blocks, increasing the MW of P3HT did not lead to the increase of D of the resulting QDs due likely to the weak coordination ability of thiophene groups of P3HT to perovskite precursors.[21] Figure 1e shows the high-resolution TEM (HRTEM) image of a P3HT-ligated $CsPbBr_3$ QD with a lattice spacing of 0.59 nm corresponding to the (001) plane of $CsPbBr_3$.[22]

For comparison, polystyrene (PS)-ligated $CsPbBr_3$ QDs and oleic acid (OA) & oleic amine (OAm)-co-capped $CsPbBr_3$ QDs (D = ∼8 nm; Figure S10) were synthesized via a modified ligand-assisted reprecipitation (LARP) method by employing amphiphilic starlike PAA-*b*-PS block copolymers as nanoreactors[22] and conventional colloidal synthesis with OA and OAm as ligands,[4] respectively. Furthermore, physically mixed P3HT/OA-&OAm-co-capped $CsPbBr_3$ QD composites (hereafter referred to as P3HT/$CsPbBr_3$ QD) was also prepared by physically mixing P3HT (MW = 5000 g/mol) and OA-&OAm-co-capped $CsPbBr_3$ QDs (D = ∼8 nm) in toluene.

To confirm the ligation of P3HT on $CsPbBr_3$ QDs, a set of studies (i.e., Fourier transform infrared spectroscopy (FT-IR), X-ray photoelectron spectroscopy (XPS), and high-resolution TEM with spherical-aberration correction under reduced electron beam voltage) were conducted (Figures S12–S14). A thin layer of P3HT with a light contrast can be seen outside the 8 nm $CsPbBr_3$ QD core with a dark contrast in Figure S14, substantiating the intimate coverage of $CsPbBr_3$ QD by the P3HT chains. Moreover, density functional theory (DFT) simulation was performed on a 3HT monomer-modified $CsPbBr_3$ slab with Pb interstitials to further understand the interaction between P3HT and $CsPbBr_3$ QD. To save computation time, the 3HT monomer was used to replace P3HT in the simulation. The projected density of states (PDOS) values of bare $CsPbBr_3$, $CsPbBr_3$ with Pb interstitials, and 3HT monomer-modified $CsPbBr_3$ with Pb interstitials were compared with the Fermi level being set to zero (Figure 2). Notably, in comparison to bare $CsPbBr_3$, the Fermi level of $CsPbBr_3$ with Pb interstitials shifts to the conduction band (CB) (Figure 2e). Moreover, a notable peak near the Fermi level in the curve of Pb p orbital ($E - E_{Fermi}$ = ∼ −0.1 eV; Figure 2e) signifies the formation of shallow levels near the CB edge,[23] which impedes charge transfer and increases the unfavorable nonradiative recombination of photogenerated charge carriers.[2] In sharp contrast, when the 3HT monomer is adsorbed at the location of Pb interstitials, the electron-donating characteristic of the S atom on the thiophene ring renders the 3HT as a Lewis base to coordinate with an additional Pb atom on the surface of $CsPbBr_3$ (a Lewis acid).[21] Specifically, the calculated absorption energy and Pb–S bond length are −0.36 eV and 3.350 Å, respectively. More importantly, the simulated PDOS of 3HT-modified $CsPbBr_3$ with Pb interstitials (Figure 2f) demonstrated that the adsorption of 3HT significantly increases the PDOS at the CB edge as evidenced by the enlarged intensity of curves shown in Figure 2f, which would improve the electrical conductivity of the 3HT-adsorbed $CsPbBr_3$ because of the passivation of Pb interstitials, thereby benefiting the charge

https://doi.org/10.1021/jacs.2c04680
J. Am. Chem. Soc. 2022, 144, 12901–12914

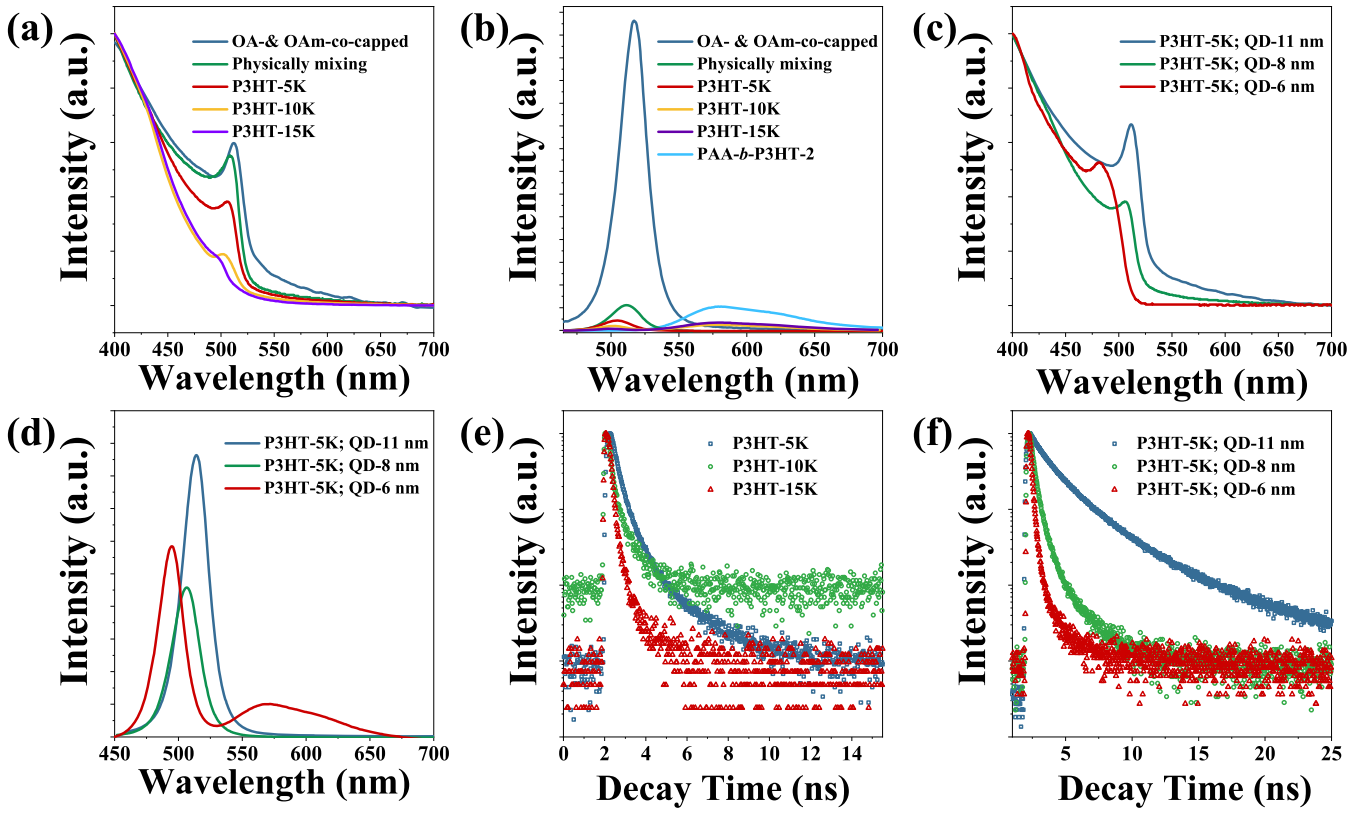

Figure 3. Optical properties of P3HT-ligated $CsPbBr_3$ QDs. (a) UV−vis absorption spectra of P3HT-ligated $CsPbBr_3$ QDs with different MWs of P3HT (5K, 10K, and 15K) and two control samples. (b) Stead-state photoluminescence (PL) spectra of three control samples and P3HT-ligated $CsPbBr_3$ QDs with different MWs of P3HT (5K, 10K, and 15K) at the same concentration. (c) UV−vis absorption spectra and (d) PL spectra of P3HT-ligated $CsPbBr_3$ QDs with different diameters (6, 8, and 11 nm) yet the same MW of P3HT (5K). Toluene was used as a solvent. Normalized time-resolved photoluminescence (TRPL) spectra of (e) P3HT-ligated $CsPbBr_3$ QDs with different chain lengths of P3HT and (f) P3HT-ligated $CsPbBr_3$ QDs with different diameters of QDs. Note that the higher background in the decay trace of the P3HT-10K sample (green dot) in (b) is due to different data collection time.

carrier transfer from perovskite to P3HT.[24] In addition, due to the incorporation (i.e., adsorption) of 3HT, the Fermi level was lifted about 0.1 eV in CB, as shown in Figure 2f, compared to that Figure 2e, indicating enhanced electrical conductivity as well as charge carrier mobility and strengthened electronic interaction between $CsPbBr_3$ and P3HT.[25] On the other hand, the C p orbitals of 3HT are well aligned to the CB of $CsPbBr_3$ and thus capable of injecting photogenerated electrons into $CsPbBr_3$ (Figure 2f), suggesting potential electron transfer from P3HT to $CsPbBr_3$ after excitation.[21] On the basis of the simulation and discussion above, the ligating of P3HT on $CsPbBr_3$ QD carries a set of advantageous effects, including defect passivation of Pb interstitials, increasing charge carrier mobility, and imparting efficient electron transfer at P3HT/$CsPbBr_3$ interface.

Steady-state UV−vis absorption spectroscopy and photoluminescence (PL) spectroscopy were then conducted to scrutinize the photophysical properties of P3HT-ligated $CsPbBr_3$ QDs (Figure 3). The band gap energies of $CsPbBr_3$ QDs were acquired via the Tauc method from steady-state UV−vis absorption spectra, while the valence bands of $CsPbBr_3$ QDs were obtained from XPS spectra (Figure S15) by following the previously reported method.[26,27] All of the $CsPbBr_3$ QDs possess the CB minimum energy and valence band (VB) maximum energy around −3.35 and −5.82 eV, respectively. On the other hand, P3HT possesses the lowest unoccupied molecular orbital (LUMO) and highest occupied molecular orbital (HOMO) at −2.6 and −4.7 eV, respectively.[28] Thus, with the electronic band levels of $CsPbBr_3$ QD shown in Figure S16, a type-II band alignment is yielded between P3HT and $CsPbBr_3$ QD in which electrons transfer from P3HT to $CsPbBr_3$ and holes transfer from $CsPbBr_3$ to P3HT. First, the effect of MWs of P3HT on the optical properties of P3HT-ligated $CsPbBr_3$ QDs was elucidated. The MWs of P3HT ligated on the surface of $CsPbBr_3$ QD are 5000, 9800, and 15,200 g/mol (hereafter referred to as 5K, 10K, and 15K; Figures 1 and S8), corresponding to approximately 30, 60, and 90 repeat units of thiophene, which is much longer than the effective conjugation length of P3HT (9−10 repeat units).[29] As a result, increasing the chain length of P3HT would not alter the position of its HOMO and LUMO.

With same diameter (i.e., D = ∼8 nm), the UV−vis absorption peak positions of OA-&OAm-co-capped $CsPbBr_3$ QDs, P3HT/$CsPbBr_3$ QD, and PH3T-ligated $CsPbBr_3$ QDs with MW of P3HT as 5K crafted by starlike block copolymer nanoreactors blue-shift from 512 to 509 and 506 nm, respectively. This can be possibly attributed to the passivation of emitting trap states at the band edge of $CsPbBr_3$ in PH3T-ligated $CsPbBr_3$ QDs rendered by the intimately tethered thiophene rings,[21] as revealed by the DFT calculation (Figure 2). After surface passivation with P3HT, the trap states near the band edge of $CsPbBr_3$ QDs are eliminated. This results in the occupancy of states situated further apart by the photogenerated charge carriers at the band edges, thereby

https://doi.org/10.1021/jacs.2c04680
J. Am. Chem. Soc. 2022, 144, 12901−12914

leading to a slight elevation of CB minimum energy (i.e., −3.37 to −3.32 eV; Figure S16a) and band gap (i.e., from 2.46 to 2.49 eV; Figure S6b) and thus a blueshift of the absorption peak position. Intriguingly, with the fixed number of P3HT chains outside $CsPbBr_3$ QD (i.e., 21 chains; due to the conversion of 21 −OH sites on β-CD into Br− terminals for ATRP of *t*BA and then click reaction with P3HT-≡), the grafting density was calculated to be 0.10 P3HT chain per nm^2 for 8 nm (i.e., 7.8 ± 0.7 nm) QDs, which is significantly lower than that of conventional OA-&OAm-co-capped $CsPbBr_3$ QDs (i.e., 3.9 oleyl species per nm^2).[30] However, compared to chloroform or chlorobenzene, P3HT has relatively poorer solubility in toluene,[20] causing the potential collapse of P3HT chains on $CsPbBr_3$ QD to passivate defects via these additional thiophene rings interacting with QD surface. Thus, even though P3HT-ligated $CsPbBr_3$ QDs have low P3HT grafting density, the collapse of P3HT chains in toluene on the surface of $CsPbBr_3$ QD in conjunction with the beneficial electron-donating nature of the S atom in thiophene ring concurrently contribute to the enhanced surface passivation of P3HT-ligated $CsPbBr_3$ QDs. As a result, further increasing the MWs of surface P3HT chains to 10K and 15K leads to a continuous blueshift to 502 and 498 nm, respectively (Figure 3a), potentially because of the increased amount of thiophene rings outside $CsPbBr_3$ QD and thus enhanced surface passivation effect.

Similar phenomena were seen in the steady-state PL spectra with an excitation wavelength of 380 nm in Figure 3b (a close-up is shown in Figure S18). The PL peak position of $CsPbBr_3$ QDs progressively blue-shifts from 517 nm in OA-&OAm-co-capped $CsPbBr_3$ QDs to 512 nm in P3HT/$CsPbBr_3$ QD, and 507 nm in P3HT-ligated $CsPbBr_3$ QDs (MW of P3HT = 5K). Notably, compared to OA-&OAm-co-capped $CsPbBr_3$ QDs and pure starlike PAA-*b*-P3HT under the same concentration, both P3HT/$CsPbBr_3$ QD and P3HT-ligated $CsPbBr_3$ QDs display markedly decreased PL intensities of $CsPbBr_3$ around 510 nm and of P3HT around 590 nm (Figure 3b). As noted above, P3HT and $CsPbBr_3$ form a staggered type-II band alignment. Thus, for P3HT-ligated $CsPbBr_3$ QDs, efficient separation of photogenerated charge carriers at the P3HT/$CsPbBr_3$ QD interface occurred, leading to quenching of PL of both P3HT and $CsPbBr_3$.[31,32]

Furthermore, increasing the MWs of P3HT from 5K to 10K and 15K in P3HT-ligated $CsPbBr_3$ QDs continuously blue-shifts the PL peak position and decreases the PL intensity of $CsPbBr_3$ QDs. In addition to the improved surface passivation by P3HT as discussed above, this phenomenon can be ascribed to more efficient charge carrier separation in $CsPbBr_3$ QDs with longer ligated P3HT chains. Specifically, the photogenerated electrons transferred from P3HT to $CsPbBr_3$ QD would increase the concentration of electrons in the QD CB and then populate in energy states higher than the CB edge due to the band filling of CB,[33] thereby blue-shifting the peak position of PL and increasing the CB minimum energy from −3.37 to −3.32 eV (Figure S16a), which is commonly known as the Moss−Burstein effect.[34] Due to the intimate contact of P3HT and $CsPbBr_3$ QD and the absence of phase segregation, P3HT-ligated $CsPbBr_3$ QDs exhibit more efficient electron transfer than P3HT/$CsPbBr_3$ QD composites, representing more obvious blueshift of the PL peak (Figure S18). As discussed above, the electronic band position of P3HT and its band alignment against $CsPbBr_3$ QD would not be changed by further increasing the MW of P3HT because of the conjugation length effect. Yet, the charge carrier mobility of P3HT has been found to be proportional to its MW owing to the increase of regioregularity in high-molecular-weight P3HT.[35] Therefore, in addition to more efficient surface passivation, the additional blueshift of the absorption peak of $CsPbBr_3$ QDs is also due likely to the more efficient electron transfer from P3HT to $CsPbBr_3$ QD with a longer length of P3HT chains. It is noteworthy that P3HT-ligated $CsPbBr_3$ QDs with a higher MW of P3HT (10K and 15K) displayed a broad PL emission of P3HT around 590 nm, corroborating the collapse and aggregation of P3HT on the $CsPbBr_3$ QD and due possibly to a relatively less efficient carrier separation in P3HT itself compared to that of $CsPbBr_3$ QDs.

The size effect of $CsPbBr_3$ QDs on the optical properties of P3HT-ligated $CsPbBr_3$ QDs was then explored. At the fixed chain length of P3HT (MW = 5K), decreasing the diameter of $CsPbBr_3$ QDs from 11 to 8 and 6 nm (Figure 1) yielded blue-shifted peaks in UV−vis absorption spectra (i.e., from 512 to 506 and 482 nm, respectively; Figure 3c) and PL spectra (i.e., from 514 to 507 and 493 nm, respectively; Figure 3d). It is important to note that $CsPbBr_3$ has an effective Bohr diameter of 7 nm,[36] experiencing the quantum confinement effect on its optical properties when the size is close to or below 7 nm.[1] Therefore, continuously downsizing from 11 to 6 nm leads to the increase of electronic band gap energy from 2.41 to 2.46 and 2.50 eV due to the quantum confinement effect (Figure S16b), which is comparable with the literature.[1]

As shown in Table S2, the 8 nm P3HT-ligated $CsPbBr_3$ QDs possessed the lowest PLQY (1.1%) compared to that of 6 nm (1.6%) and 11 nm (6.2%) P3HT-ligated $CsPbBr_3$ QDs. Notably, the quantum confinement effect in $CsPbBr_3$ QDs yields enlarged band-gap energy via upward and downward shifting of CB edge and VB edge (Figure S16), respectively,[4] and a high PLQY of $CsPbBr_3$ QDs owing to enhanced exciton binding energy.[37] Therefore, from 11 to 8 nm, the energy difference between the VB edge of $CsPbBr_3$ QDs and the HOMO of P3HT was increased, leading to an enhanced driving force for the transfer of photogenerated holes from $CsPbBr_3$ QDs to P3HT and thus decreased PLQY (1.1%). However, further decreasing the size of $CsPbBr_3$ QDs from 8 to 6 nm introduced a strong quantum confinement on 6 nm $CsPbBr_3$ QDs,[1,36] which may slightly overwhelm the enhanced charge separation resulting from further VB edge down-shifting, thereby yielding a higher PLQY of 6 nm P3HT-ligated $CsPbBr_3$ QDs than 8 nm P3HT-ligated $CsPbBr_3$ QDs.

To further scrutinize the charge separation process in P3HT-ligated $CsPbBr_3$ QDs, time-resolved PL (TRPL) measurements were performed at the detecting wavelength of 505 nm (Figure 3e,f). For comparison, TRPL spectra of OA-&OAm-co-capped $CsPbBr_3$ QDs and physically mixed P3HT/$CsPbBr_3$ QD composites were also recorded (Figure S19). The TRPL data were fitted with a biexponential decay model containing a fast decay time component τ_1 (intrinsic band-to-band recombination of photogenerated charge carriers) and a slow decay time component τ_2 (trap-assisted recombination)[37] (see the Supporting Information for more details). As shown in Tables S1 and S2, all P3HT-ligated $CsPbBr_3$ QDs manifested shorter PL lifetimes than those of OA-&OAm-co-capped $CsPbBr_3$ QDs and physically mixed P3HT/$CsPbBr_3$ QD composites. Specifically, the intimate contact between P3HT and $CsPbBr_3$ in P3HT-ligated $CsPbBr_3$ QDs led to a significantly decreased τ_1 (e.g., 0.31 ns for 8 nm QDs with P3HT-5K) compared to OA-&OAm-co-capped

https://doi.org/10.1021/jacs.2c04680
J. Am. Chem. Soc. 2022, 144, 12901−12914

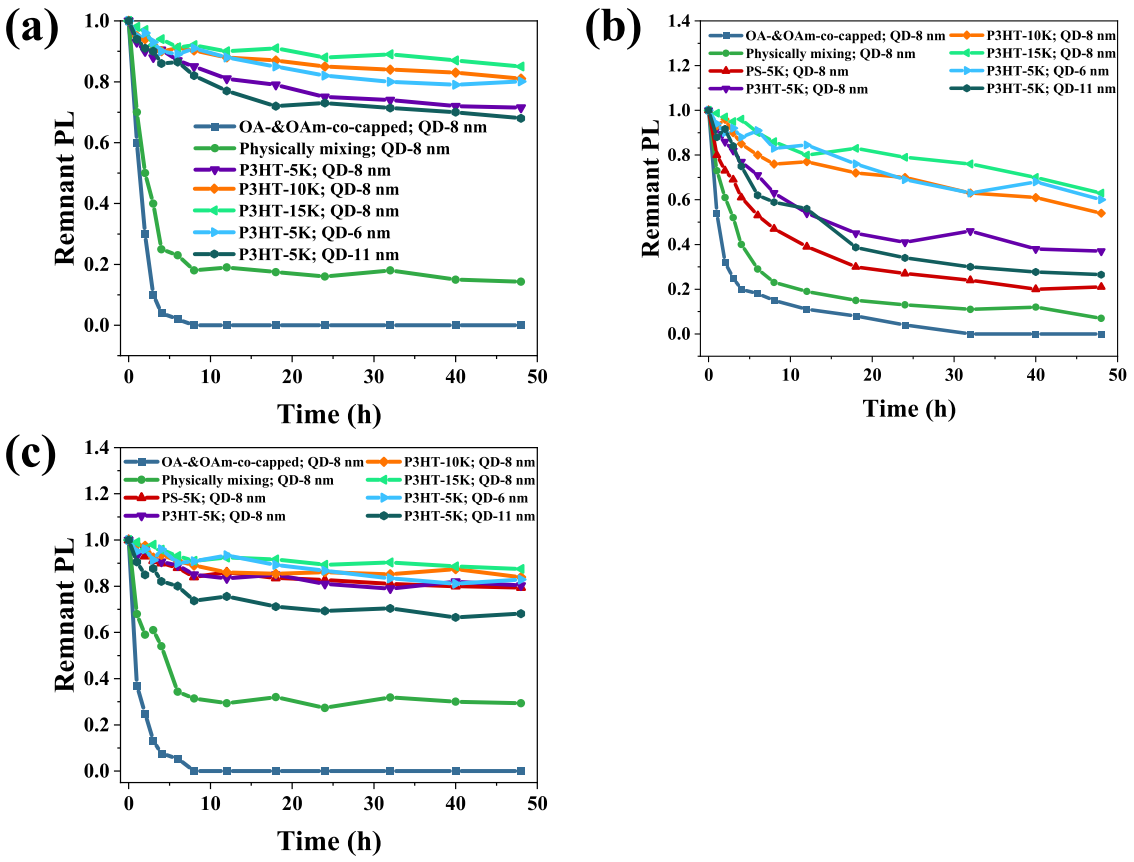

Figure 4. Stability of P3HT-ligated $CsPbBr_3$ QDs. (a) Thermal stability, (b) UV irradiation stability, and (c) polar solvent stability of P3HT-ligated $CsPbBr_3$ QDs with varied sizes of QDs (6, 8, and 11 nm) and chain lengths of P3HT (5K, 10K, and 15K). Control samples of OA-&OAm-co-capped $CsPbBr_3$ QDs, physically mixed P3HT/$CsPbBr_3$ QD composites, and PS-ligated $CsPbBr_3$ QDs are also included for comparison.

$CsPbBr_3$ QDs (τ_1 = 1.67 ns) and physically mixed P3HT/$CsPbBr_3$ QD composites (τ_1 = 2.10 ns). On the basis of the DFT calculation (Figure 2) and UV−vis spectra and PL spectra (Figure 3), the ligating of P3HT did not introduce additional surface defects and instead rendered effective surface passivation. Therefore, the decrease in PL decay lifetimes can be attributed to the presence of new decay pathways for photogenerated charge carriers,[38] i.e., hole transfer to the HOMO of P3HT, further substantiating the effective charge carrier separation at the P3HT/$CsPbBr_3$ QD interfaces.[32] Notably, similar fast transfers of charge carriers of $CsPbBr_3$ QDs interfaced with either molecular donor or acceptor have been reported in the literature.[32] With the presence of potential phase segregation and absence of intimate contact, P3HT/$CsPbBr_3$ QD composites exhibited a similar τ_1 compared to that of OA-&OAm-co-capped $CsPbBr_3$ QDs, possibly owing to insufficient charge carrier transfer at their interface. As a result, directly tethering P3HT outside individual $CsPbBr_3$ QD for constructing homogeneous nanocomposites is of critical importance to impart efficient charge carrier transfer. On the other hand, increasing the MW of ligated P3HT chains led to even faster PL decay (Figure 3e and Table S1), suggesting improved charge carrier mobility in high-MW P3HT chains indeed contributes to more efficient charge carrier separation at the P3HT/$CsPbBr_3$ QD interfaces as discussed above.

The PL decay of $CsPbBr_3$ QDs with different QD sizes at the same length of ligated P3HT chains was also investigated (Figure 3f and Table S2). Similar to the findings from the steady-state UV−vis and PL spectra (Figure 3c,d), the decrease in the diameter of $CsPbBr_3$ QDs resulted in faster PL decay, signifying the strong quantum confinement effect[37] and efficient charge carrier separation in smaller-size P3HT-ligated $CsPbBr_3$ QDs.[38] This is not surprising as the stronger quantum confinement effect in smaller QDs shifts the VB edge of $CsPbBr_3$ to more positive potentials (Figure S16a), increasing the driving force for hole transfer to P3HT, and increases the coupling strength for hole transfer.[38]

As discussed above, in addition to efficient separation of photogenerated charge carriers, the other key characteristic is the stability of perovskite QDs. This is because the ability to reliably improve it while retaining their single nanoparticle aspect without aggregation represents a crucial step for their practical applications in optoelectronics and photocatalysis. In this context, the stabilities of P3HT-ligated $CsPbBr_3$ QDs under different conditions were examined, including exposing to elevated temperature to evaluate thermal stability, mixing with a small portion of isopropanol to inspect polar solvent stability, and UV irradiation to assess photostability (Figure 4).

First, the thermal stability of as-crafted $CsPbBr_3$ QDs was explored via heating the QD toluene solution to 70 °C and keeping it for a certain period of time (Figure 4a). Typically, conventional OA-&OAm-co-capped $CsPbBr_3$ QDs exhibited a considerable PL intensity drop after maintaining the solution at 70 °C for 5 h, possibly owing to pronounced trapping of charge carriers[37] as well as aggregation of QDs caused by dissociation of small molecular ligands (OA and OAm) at high temperatures.[1,4,36] A physical mixture of P3HT/$CsPbBr_3$ QDs

https://doi.org/10.1021/jacs.2c04680
J. Am. Chem. Soc. 2022, 144, 12901−12914

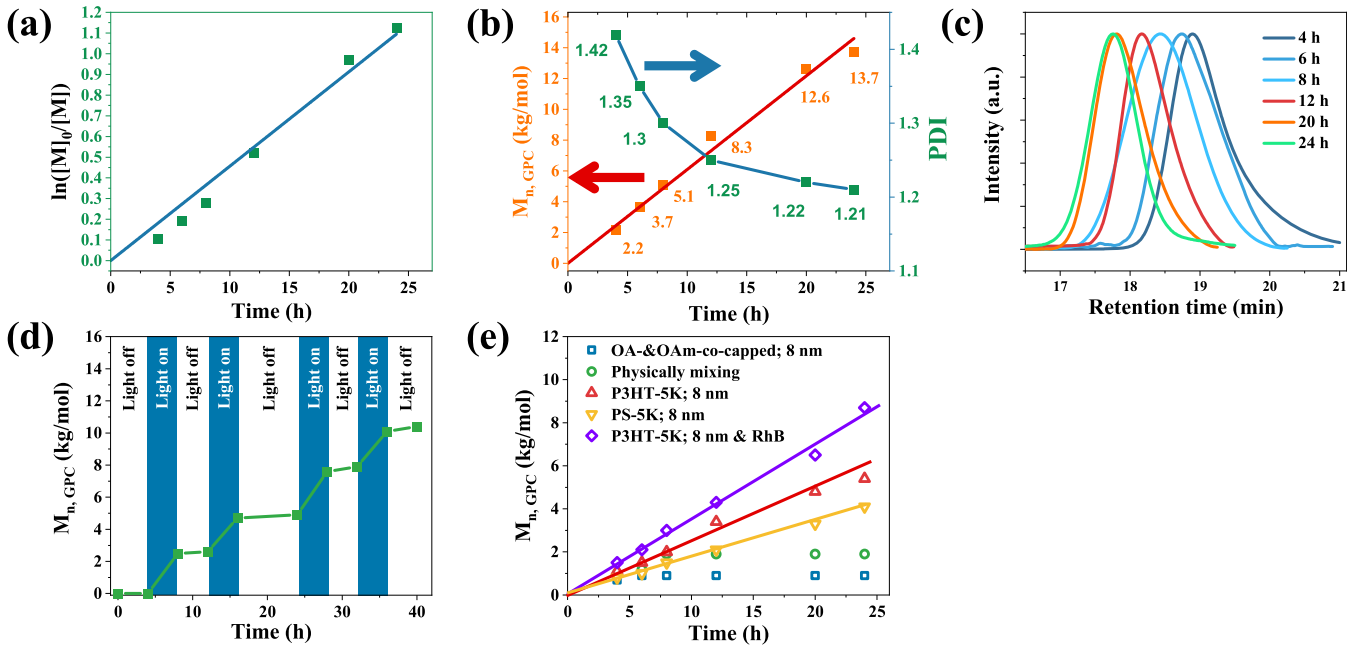

Figure 5. P3HT-ligated $CsPbBr_3$ QDs for photocatalyzing ATRP. (a) Semilogarithmic kinetic plot of photoinduced ATRP (p-ATRP) catalyzed by P3HT-ligated $CsPbBr_3$ QDs. (b) Evolution of number-average MW (M_n) and polydispersity index (PDI) of p-ATRP of MMA monomers. (c) GPC traces of the resulting PMMA with time. (d) Temporal control of the M_n of PMMA in p-ATRP catalyzed by P3HT-ligated $CsPbBr_3$ QDs. (e) Comparisons of evolution of M_n of p-ATRP of MMA catalyzed by different photocatalysts.

yielded improved stability due to the protection of the P3HT matrix over $CsPbBr_3$ QDs, yet still presented a significant loss of PL in less than 10 h. In stark contrast, all P3HT-ligated $CsPbBr_3$ QDs rendered remarkably enhanced retention of PL at 70 °C for 48 h (i.e., PL retention of 69% for 8 nm QDs ligated with P3HT of 5K per arm and of 85% for 8 nm $CsPbBr_3$ QDs ligated with P3HT of 15K per arm). The capability of introducing intimate and permanent P3HT ligation ensures the creation of a stable protective polymer shell over $CsPbBr_3$ QD at the single-particle level, thereby eliminating the issues associated with the dissociation of ligands and thus incomplete surface ligand coverage. As such, the PL loss of $CsPbBr_3$ QDs was clearly retarded.

Subsequently, the photostability of $CsPbBr_3$ QDs against UV light irradiation (wavelength of 365 nm and intensity of 50 mW) was studied. Conventional OA-&OAm-co-capped $CsPbBr_3$ QDs were found to undergo a rapid drop of PL intensity to 20% in 4 h and complete quenching of PL in 32 h due to UV-induced decomposition of $CsPbBr_3$ QDs (Figure 4b). In marked contrast, 8 nm $CsPbBr_3$ QDs ligated with long P3HT chains (MW = 15K) retained 63% of original PL intensity after 48 h illumination, suggesting superior photostability of P3HT-ligated $CsPbBr_3$ QDs under intensive UV irradiation. Moreover, compared to PS-ligated $CsPbBr_3$ QDs where PS chains have no absorption at 365 nm, P3HT chains in P3HT-ligated $CsPbBr_3$ QDs absorb the 365 nm UV[31] and thus was able to attenuate the UV light intensity that reached $CsPbBr_3$ QDs. Therefore, the remanence PL of $CsPbBr_3$ QDs was increased from 21% in PS-ligated $CsPbBr_3$ QDs to 37% in P3HT-ligated $CsPbBr_3$ QDs with the same MW of PS and P3HT. With the fixed number of P3HT chains ligated (i.e., 21 chains as noted above), the photostability of P3HT-ligated $CsPbBr_3$ QDs was seen to be further enhanced by either increasing the chain length of P3HT or increasing the grafting density of P3HT via decreasing the size of QDs (e.g., from 0.067 P3HT chain per nm^2 in 11 nm $CsPbBr_3$ QDs to 0.186 P3HT chain per nm^2 in 6 nm $CsPbBr_3$ QDs) (Figure 4b), demonstrating the great potential of capitalizing on this unique class of nanomaterials as stable photocatalysts, as discussed below.

The polar solvent stability of as-prepared $CsPbBr_3$ QDs was then appraised via injecting isopropanol into the QDs toluene solution at 10% volume ratio under vigorous stirring. It is well known that perovskites are prone to structurally disintegrate in high-polarity solvents (e.g., water, methanol, isopropanol, etc.) due to their ionic crystal nature, resulting in degradation of QDs and quenching of PL.[3] As shown in Figure 4c, conventional OA-&OAm-co-capped $CsPbBr_3$ QDs manifested continuous diminishing of PL after exposing to isopropanol within a few hours and complete loss of PL after 8 h. A physical mixture of P3HT/$CsPbBr_3$ QDs yielded improved polar solvent stability over that of OA-&OAm-co-capped $CsPbBr_3$ QDs, indicating the presence of polymer matrix limited the direct contact of $CsPbBr_3$ QDs with polar solvent. Nevertheless, the much worse polar solvent stability of physically mixed P3HT/$CsPbBr_3$ QD composites than that of P3HT-ligated $CsPbBr_3$ QDs signifies that the potentially incomplete and loose surface capping of P3HT on QD and possible aggregation of QDs in the P3HT matrix for the physically mixed P3HT/$CsPbBr_3$ QD composites could afford only limited protection of $CsPbBr_3$ QDs against polar solvent. In stark contrast, all P3HT-ligated $CsPbBr_3$ QDs survived in such deleterious polar environment with a maximum 87.5% retention of PL intensity (i.e., for 8 nm P3HT-ligated $CsPbBr_3$ QDs with the MW of P3HT of 15K) after 48 h. Interestingly, the 8 nm P3HT-ligated $CsPbBr_3$ QDs displayed a similar remanence of PL intensity to PS-ligated $CsPbBr_3$ QDs, possibly owing to the poor solubility of both P3HT and PS (having the same MW) in isopropanol.[20,22] The immiscibility of P3HT and PS in isopropanol leads to the collapse of

https://doi.org/10.1021/jacs.2c04680
J. Am. Chem. Soc. 2022, 144, 12901−12914

polymer chains on the surface of QD, thereby forming a densely packed protective shell on the single-particle level to effectively hinder the diffusion of isopropanol to reach $CsPbBr_3$ QDs. It is worth noting that increasing the MW of P3HT from 5K to 10K and 15K imparts denser hydrophobic P3HT shell situated on the $CsPbBr_3$ QD, thus more adequately blocking the penetration of isopropanol and leading to enhanced retention of PL from 81 to 86.1 and 89.3%, respectively. On the other hand, decreasing the size of QDs at the fixed length of P3HT manifested markedly enhanced remanence of PL from 69.3% in 11 nm $CsPbBr_3$ QDs to 86.7% in 6 nm $CsPbBr_3$ QDs, which is likely due to the increased grafting density of P3HT chains as discussed above.

The appealing set of attributes of P3HT-ligated $CsPbBr_3$ QDs (i.e., tunable optical properties, efficient charge carriers separation, and outstanding stabilities), all depending heavily on the size of $CsPbBr_3$ QDs and the length of P3HT chains, which can be conveniently tailored via starlike block copolymer nanoreactor strategy, may poise them as promising candidates for p-ATRP reaction of a wide range of monomers to yield polymers with narrow MW distribution. In this context, such p-ATRP was first demonstrated using P3HT-ligated $CsPbBr_3$ QDs as the photocatalyst, ethyl α-bromoisobutyrate (EBiB) as the initiator, 4,4′-dinonyl-2,2′-dipyridyl (dNBpy) as the ligand, $CuBr_2$ as the co-catalyst, and methyl methacrylate (MAA) as the monomer under the irradiation of UV light (λ = 385 nm) (Figure 5). As shown in entry 1 (Table S3), the p-ATRP of MAA in toluene yielded a monomer conversion of 28% (comparable to other p-ATRP[8,10,11]), a predictable number-average MW (M_n = 5400 g/mol), and a low polydispersity index (PDI = 1.21) after 24 h of 20 mW/cm^2 UV light irradiation at room temperature, exemplifying the effectiveness of P3HT-ligated $CsPbBr_3$ QDs as photocatalysts for well-controlled p-ATRP. Moreover, a set of control experiments (entries 2−7, Table S3) were carried out to reveal that the Cu(II)Br_2 co-catalyst, dNBpy ligand, P3HT-ligated $CsPbBr_3$ QDs, and UV light irradiation were indispensable for successful p-ATRP of MMA. The absence of any one of them led to no polymerization of MMA at room temperature after 24 h, substantiating that the p-ATRP was unambiguously photocatalyzed by P3HT-ligated $CsPbBr_3$ QDs. In addition, heating the reaction mixture at an elevated temperature (50 °C) without light irradiation (entry 7, Table S3) did not produce any PMMA, suggesting the successful polymerization in entry 1 was not thermally initiated by irradiation-induced heating.

Notably, in addition to toluene (a relative polarity of 0.099), anisole (a relative polarity of 0.198) and tetrahydrofuran (THF) (a relative polarity of 0.21) were also used as the solvents for p-ATRP (entries 14 and 15, respectively; Table S3). Nonetheless, due to the poorer solubility of P3HT in anisole than in toluene and the higher polarity of anisole than toluene,[20] the potential degradation of QDs and insufficient contact between QDs and Cu(II)Br_2 co-catalyst led to a slower reaction kinetics and a decreased monomer conversion in anisole. On the other hand, even though polar solvents were found to be beneficial for p-ATRP,[11] THF with high polarity and good solubility of P3HT may result in severe degradation of QDs, thereby invoking much lower monomer conversion and significantly large PDI (1.53). Additionally, several monomers (i.e., *t*BA, methyl acrylate (MA), and styrene (St)) other than MMA were successfully polymerized as well (entries 16−19, Table S3), revealing the versatility and effectiveness of p-ATRP by capitalizing on P3HT-ligated $CsPbBr_3$ QDs as photocatalysts. Remarkably, even under elevated temperature, due to enhanced thermal stability as discussed above, P3HT-ligated $CsPbBr_3$ QDs were still capable of p-ATRP of St, yielding a monomer conversion of 17% and low PDI of 1.20 (entry 19, Table S3).

Afterward, the reaction kinetics of p-ATRP of MMA was explored by taking a small amount of the reaction mixture at a specific time period under the same conditions as entry 9 in Table S3. Figure 5a depicts the semilogarithmic plot of monomer concentration versus reaction time with a linear behavior. This suggests a constant concentration of propagation radicals in p-ATRP, a characteristic of ATRP as controlled radical polymerization,[39] and the absence of deleterious side reactions (e.g., chain termination and intermolecular coupling). Moreover, the M_n of PMMA also underwent a linear increase with reaction time upon light irradiation (Figure 5b), in good agreement with theoretical expectations based on the calculation of monomer conversion from ^{1}H NMR, demonstrating the fine control of polymerization. However, it is worth noting that the initial PDIs of as-synthesized PMMA are relatively broad (i.e., 1.42 after 4 h and 1.35 after 6 h p-ATRP). The monomodal peaks in the GPC traces manifest the absence of intermolecular coupling of as-synthesized PMMA, indicating that the limited initiation efficiency may account for the broadening of PDI at the beginning of p-ATRP.[39] Moreover, the appearance of tails in the GPC traces of the initial three samples (Figure 5c) corroborated the occurrence of slow initiation of p-ATRP as well. The reasons causing this phenomenon can probably be attributed to the low amount of active Cu(I)Br catalyst present and a small value of the Cu(I)/initiator (i.e., EBiB) ratio at the early stage of the reaction due to insufficient charge transfer from P3HT-ligated $CsPbBr_3$ QDs to dormant Cu(II)Br_2 species, which is commonly seen in other p-ATRPs.[10] By exposing the reaction mixture to light irradiation of higher intensity (i.e., entries 1 and 13 versus entries 11 and 12; Table S3) or adding more P3HT-ligated $CsPbBr_3$ QDs (i.e., entries 1 and 8 versus entries 9 and 10; Table S3), the drop of PDI for the final products clearly demonstrated their abilities to expedite initiation via generating extra charge carriers at the beginning of polymerization for the photoreduction of Cu(II)Br_2. Furthermore, at low monomer conversion, the variation in the number of monomer addition per the activation/deactivation cycle in ATRP would be more pronounced as predicted by both theoretical modeling and prior experiments, resulting in broad PDI at the initial stage of the polymerization, followed by low PDI at the later propagation-dominant stages.[39] As a result, similar to typical ATRP reactions, the PDI of as-prepared PMMA decreased as the monomer conversion increased (Figure 5b), and the GPC traces became more symmetrical and continuously shifted toward higher MW as the polymerization progressed (Figure 5c), providing further evidence of well-controlled p-ATRP.

It is also noteworthy that the p-ATRP catalyzed by P3HT-ligated $CsPbBr_3$ QDs exerted excellent temporal control over MW (Figure 5d). Typically, the MW of PMMA increased linearly under the exposure to UV light and ceased to grow after switching off the irradiation. Upon restarting the irradiation, the polymer chain propagation continued and yielded higher MW of PMMA, signifying a high degree of temporal control in p-ATRP for reversible activation/deactivation cycle[9] conveniently rendered by P3HT-ligated $CsPbBr_3$ QDs photocatalysts.

https://doi.org/10.1021/jacs.2c04680
J. Am. Chem. Soc. 2022, 144, 12901−12914

Table 2. Results of Photoinduced ATRP (p-ATRP) of MMA with Various $CsPbBr_3$ QDs as Photocatalysts under the Same Reaction Conditions[a]

entry	$CsPbBr_3$ QDs[b]	pure P3HT homopolymer (wt %)[c]	RhB (wt %)[c]	conv. (%)[d]	$M_{n,th}$[e]	$M_{n,GPC}$[f]	PDI[f]
1	OA-&OAm-co-capped QD-8 nm			<5	1200	900	1.51
2	physically mixed QD-8 nm			10	2200	1900	1.43
3	PS-5K; QD-8 nm			19	4000	4100	1.28
4	P3HT-5K; QD-8 nm			28	5800	5400	1.21
5	P3HT-10K; QD-8 nm			39	8000	9300	1.19
6	P3HT-15K; QD-8 nm			57	11,600	12,100	1.22
7	P3HT-5K; QD-6 nm			51	10,400	11,300	1.15
8	P3HT-5K; QD-10 nm			22	4600	3900	1.21
9			0.05	<1			
10	P3HT-5K; QD-8 nm		0.05	39	8000	8700	1.17
11		0.5		<1			

[a]General reaction condition: [MMA] (monomer)/[EBiB] (initiator)/[$CuBr_2$] (co-catalyst)/[dNBpy] (ligand)/[Solvent] = 200:1:0.5:1:400 (molar ratio) under irradiation of 385 nm UV light at room temperature for 24 h. [b]The amount of $CsPbBr_3$ QDs added into the reaction was fixed at 0.5% by weight of monomers. [c]wt % represents the weight percentage to monomers. [d]Conversion was determined by ^1H NMR in $CDCl_3$. [e]Theoretical number-average molecular weight of polymer calculated on the basis of conversion (i.e., $M_{n,th} = M_{EBiB} + 200 \times \text{conversion} \times M_{monomer}$). [f]Measured number-average molecular weight of polymer from GPC with THF as mobile phase and linear PS as calibration standard.

We then turn our attention to unravel the effects of QD stability, charge carrier separation, and QD size on p-ATRP by employing various P3HT-ligated $CsPbBr_3$ QDs to p-ATRP of MMA under identical conditions (Table 2). First, the use of conventional OA-&OAm-co-capped $CsPbBr_3$ QDs as photocatalysts showed a limited MMA monomer conversion of less than 5% after 24 h of polymerization and a large PDI of 1.51 (entry 1, Table 2). The M_n of PMMA remained unchanged after 4 h of polymerization with OA-&OAm-co-capped $CsPbBr_3$ QD photocatalysts (Figure 5e), suggesting that the decomposition of QDs inhibited the further polymerization of MMA. Similarly, despite better UV stability as discussed above, physically mixed P3HT/$CsPbBr_3$ QD composites only had a slightly improved lifetime of $CsPbBr_3$ QDs, thus allowing for continuous polymerization for approximately 6 h and a relatively higher monomer conversion of 10%. In sharp contrast, linear growth of M_n and higher monomer conversion of PMMA in Figure 5e (red and yellow curves) and Table 2 (entries 3−8), respectively, signify the viability of polymer-ligated $CsPbBr_3$ QDs (both PS-ligated and P3HT-ligated) in the reaction mixture under continuous irradiation for 24 h. Clearly, crafting highly stable $CsPbBr_3$ QDs with permanently ligated, protective polymer shell at the single-particle level is of key importance and highly beneficial for the application of $CsPbBr_3$ QDs in photocatalysis.

Subsequently, the effect of charge carrier separation on the efficiency of p-ATRP was explored. As OA-&OAm-co-capped $CsPbBr_3$ QDs were prone to be degraded under strong UV light irradiation, both PS-ligated and P3HT-ligated $CsPbBr_3$ QDs with the same MW of PS and P3HT (5K per arm) were chosen as photocatalysts. For PS-ligated $CsPbBr_3$ QDs, charge carriers can be generated in $CsPbBr_3$ QDs and used for p-ATRP. Interestingly, despite the inability to impart charge separation at the PS/$CsPbBr_3$ QD interfaces due to the insulating nature of PS, PS was capable of withstanding continuous light irradiation as indicated in the linear MW increase (yellow curve, Figure 5e), endowing relatively slow kinetics and low monomer conversion after 24 h reaction (entry 3, Table 2). By contrast, the efficient charge carrier separation at the P3HT/$CsPbBr_3$ QD interfaces markedly promoted the polymerization kinetics, as evidenced by the red curve in Figure 5e, and yielded a higher monomer conversion under identical condition, corroborating the advantageous attributes of ligating semiconducting CPs as ligands on the $CsPbBr_3$ QD surface. Moreover, in comparison to physically mixed P3HT/$CsPbBr_3$ QD composites, the synergy of outstanding stabilities and enhanced charge carrier separation of P3HT-ligated $CsPbBr_3$ QDs due to the intimate and firm tethering of P3HT chains rendered several beneficial outcomes, including the longer lifetime of the resulting $CsPbBr_3$ QD photocatalysts, more efficient p-ATRP, and better control over the PDI of the as-prepared polymer via p-ATRP. Further boosting charge carrier separation efficiency via increasing the P3HT chain length as discussed above enabled even higher monomer conversions after 24 h (entries 5 and 6 versus entry 4, Table 2) in p-ATRP, verifying that the charge carrier dynamics of $CsPbBr_3$ QDs can be meticulously tailored via surface engineering of conjugated ligands of different MW for robust photocatalysis. Notably, pure P3HT homopolymer with MW of 5000 g/mol was also utilized in p-ATRP as the control sample. As shown in entry 11 (Table 2), no polymerization of MMA can be seen, thereby excluding the potential photocatalytic polymerization induced via photoreduction of Cu(II)Br_2 by P3HT. Thus, the enhanced kinetics and monomer conversion of p-ATRP of MMA was not due to the presence of an additional light harvester (i.e., P3HT) but a set of favorable characteristics of P3HT-ligated $CsPbBr_3$ QDs noted above.

The influence of the size of P3HT-ligated $CsPbBr_3$ QDs on p-ATRP was then examined. The change of QD size was found to alter its photocatalytic reactivity. Specifically, the 6 nm P3HT-ligated $CsPbBr_3$ QDs possessed the highest charge carrier separation efficiency as evidenced by the lowest τ_{avg} and the highest k_{nr} (Table S2), and thus yielded the highest monomer conversion (51%; see entry 7 in Table 2) in p-ATRP after 24 h. On the other hand, the 11 nm P3HT-ligated $CsPbBr_3$ QDs with relatively less efficient charge carrier separation and possibly larger light scattering of QD[11] than those of 8 and 6 nm QDs due to the increased size only produced 22% of monomer conversion in p-ATRP (entry 8, Table 2), further reinforcing the importance of efficient charge carrier separation in photocatalytic polymerization.

To demonstrate the effectiveness of exploiting P3HT-ligated $CsPbBr_3$ QDs as photocatalyst in p-ATRP, 8 nm CdSe QDs were also synthesized by employing starlike PAA-*b*-P3HT-2

https://doi.org/10.1021/jacs.2c04680
J. Am. Chem. Soc. 2022, 144, 12901−12914

block copolymer as nanoreactor as well as by using small molecular organic ligands (i.e., tri-*n*-octylphosphine oxide (TOPO))[40] (see the Supporting Information). The typical TEM images of TOPO-capped and P3HT-ligated CdSe QDs with uniform morphology and similar dimension of approximately 8 nm are shown in Figure S20. Subsequently, these two types of CdSe QDs were applied as photocatalysts in the p-ATRP of MMA under the same conditions as entry 1 in Table S3. The results of p-ATRP of MMA and the corresponding evolution of M_n of p-ATRP of PMMA can be seen in Table S4 and Figure S21. For comparison, the evolution of M_n of p-ATRP of MMA from 8 nm P3HT-5K-ligated $CsPbBr_3$ QDs (entry 4 in Table 2) and 8 nm PS-5K-ligated $CsPbBr_3$ QDs (entry 3) shown in Figure 5e was also included in Figure S21.

Specifically, both TOPO-capped and P3HT-ligated CdSe QDs function as photocatalysts in p-ATRP of MMA. Compared to OA-&OAm-ligated $CsPbBr_3$ QDs, conventional TOPO-capped CdSe QDs with improved intrinsic stability under UV irradiation could continuously photocatalyze the p-ATRP of MMA for 24 h. However, TOPO-capped CdSe QDs rendered a lower conversion (11%) than that of P3HT-ligated $CsPbBr_3$ QDs (28%) and CdSe QDs (22%) after the same period of reaction time, due likely to the absence of efficient charge carriers separation at the TOPO/CdSe interface. On the other hand, the evolution of M_n of PMMA catalyzed by TOPO-capped CdSe QDs (i.e., blue squares in Figure S21) did not follow a linear growth that is commonly seen in ATRP. As reported in a previous study,[41] TOPO ligands may undergo the ligand dissociation from the QD surface in solution, thereby creating defects on the CdSe surface and leading to inevitable aggregation of QDs. As a result, charge carrier transfer from TOPO-capped CdSe QDs to $Cu(II)Br_2$ was retarded, resulting in declined reaction kinetics and relatively low conversion of monomer of p-ATRP, which is similar to the case of p-ATRP using OA-&OAm-co-capped $CsPbBr_3$ QDs.

In contrast, QDs with permanent ligation of polymer chains (i.e., PS-ligated $CsPbBr_3$ QDs in yellow, P3HT-ligated CdSe QDs in green, and P3HT-ligated $CsPbBr_3$ QDs in red; Figure S21) imparted linear growth of M_n, suggesting that the QDs with perpetual tethering of polymer shell rendered the enhanced stability and stable interaction with $Cu(II)Br_2$. Compared to PS-ligated $CsPbBr_3$ QDs, P3HT-ligated CdSe QDs afforded a higher monomer conversion and faster reaction kinetics. As previously reported, the formation of type-II electronic band alignment between P3HT and CdSe also produces charge carrier separation at their interface,[31] thereby promoting the kinetics of p-ATRP. However, the reaction kinetics and monomer conversion of p-ATRP catalyzed by P3HT-ligated CdSe QDs are slower than that of P3HT-ligated $CsPbBr_3$ QDs (Figure S21), which may be attributed to a distinctive band alignment between CdSe QDs and P3HT.

The 8 nm CdSe QDs possess a CB minimum energy of −3.6 eV and a VB maximum energy of −5.9 eV.[42,43] Based on the electronic band alignment, P3HT-ligated $CsPbBr_3$ QDs exhibited a smaller offset (i.e., 0.75 eV) between the CB minimum energy of $CsPbBr_3$ and the LUMO of P3HT than that of P3HT-ligated CdSe QDs (i.e., 1.0 eV) between the CB minimum energy of CdSe and the LUMO of P3HT. In this context, the larger offset of the latter may yield a slower electron transfer from P3HT to CdSe than that of the former (from P3HT to $CsPbBr_3$), thereby leading to a relatively lower monomer conversion and slower kinetics of p-ATRP. Clearly, the major advantages of P3HT-ligated $CsPbBr_3$ QDs over conventional CdSe QDs manifested in their improved stability and stabile electronic interaction with $Cu(II)Br_2$ due to the absence of ligand dissociation, as well as higher efficiency in p-ATRP as a result of more effective charge carrier separation at the P3HT/$CsPbBr_3$ interface.

Notably, the mechanism of QD-enabled p-ATRP has been explored both experimentally and theoretically[44,45] and considered to be driven by either electron transfer or energy transfer process. Typically, QDs function as a light harvester to absorb incident irradiation and generate charge carriers that can be directly transferred to $Cu(II)Br_2$ to induce reduction and formation of Cu(I)Br (electron transfer process), or undergo radiative decay to emit light with proper wavelength, which can be absorbed by $Cu(II)Br_2$/ligand complex to generate Cu(I)Br (energy transfer process). As shown in Figure S22, the PL spectra of P3HT-ligated $CsPbBr_3$ QDs exhibited no overlapping with the absorption peak of the $Cu(II)Br_2$/dNBpy complex in toluene, excluding the potential energy transfer-based mechanism for p-ATRP investigated above. To scrutinize whether photogenerated holes or electrons play as active species in p-ATRP, rhodamine B (RhB), a commercially available organic dye, that normally acts as an electron acceptor was added into the reaction mixture containing P3HT-ligated $CsPbBr_3$ QDs. The energy-level diagram of P3HT, $CsPbBr_3$ QDs, and RhB as well as the standard redox potential of Cu^{2+}/Cu^{+} reaction (−4.6 eV) is illustrated in Figure S23.[28,38,44] Specifically, as the HOMO of P3HT located at −4.7 eV and is less negative than the VB edge of $CsPbBr_3$ QDs (i.e., −5.82 eV from averaging VB of all QDs in Figure S16a), P3HT functions as the hole acceptor in P3HT-ligated $CsPbBr_3$ QDs. On the other hand, the LUMO of P3HT (−2.6 eV) is less negative than the CB edge of $CsPbBr_3$ QDs (i.e., −3.35 eV from averaging CB of all QDs in Figure S16a), suggesting a potential electron injection from P3HT to $CsPbBr_3$. Moreover, in the P3HT-ligated $CsPbBr_3$ QDs/RhB mixture, RhB with negligible absorption at 385 nm and its LUMO located at −3.9 eV produces no additional photogenerated charge carriers under UV light irradiation, yet acts as an electron acceptor to obtain photogenerated electrons from $CsPbBr_3$ QDs. Therefore, if the addition of RhB alters the p-ATRP reaction kinetics, the electron is then substantiated to be the active species that drives the entire reaction. Furthermore, in the absence of P3HT-$CsPbBr_3$ QDs, pure RhB was utilized for p-ATRP under identical conditions as discussed above (control experiment). As shown in entry 9 in Table 2, no polymerization can be detected, indicating RhB alone cannot induce ATRP under UV light irradiation and thus excluding the potential RhB-induced photocatalytic ATRP.

Intriguingly, the addition of a trace amount of RhB in the reaction mixture containing 8 nm P3HT-ligated $CsPbBr_3$ QDs (MW of P3HT per arm = 5K) yielded faster reaction kinetics and higher monomer conversion after 24 h (purple curve in Figure 5e and entry 10 in Table 2, respectively) than that of pure P3HT-ligated $CsPbBr_3$ QDs (red curve in Figure 5e and entry 4 in Table 2, respectively), thereby providing compelling evidence for the hypothesis mentioned above and concurring to previous electron transfer-driven mechanism in p-ATRPs.[44,45] Clearly, the incorporation of RhB as an electron acceptor afforded an additional electron-transport pathway for electrons situated at the CB edge of $CsPbBr_3$ QDs, leading to more efficient charge carrier separation and suppressed radiative recombination.

https://doi.org/10.1021/jacs.2c04680
J. Am. Chem. Soc. 2022, 144, 12901−12914

On the basis of the discussion above, the mechanism of P3HT-ligated $CsPbBr_3$ QD-catalyzed p-ATRP can be rationalized as follows (Figure S24). Typically, P3HT-ligated $CsPbBr_3$ QDs experience photoexcitation under UV light irradiation and generate charge carriers on both P3HT and $CsPbBr_3$ QDs. Afterward, charge separation efficiently occurs at the P3HT/$CsPbBr_3$ QD interfaces to populate electrons at the CB of $CsPbBr_3$ QDs and holes at the HOMO of P3HT. Subsequently, electron transfer from $CsPbBr_3$ QDs to the Cu(II)Br_2/ligand complex reduces the dormant Cu(II) to active Cu(I), thus initiating living radical polymerization from alkyl bromide initiator (EBiB). On the other hand, bromine anion from Cu(II)Br_2 is first donated to P3HT-ligated $CsPbBr_3$ QDs, followed by transferring to the chain end of polymer, leading to the regeneration of P3HT-ligated $CsPbBr_3$ QDs, similar to the previous reports of employing other types QDs for p-ATRP.[8]

CONCLUSIONS

In summary, we demonstrated the robustness of tailoring the dimension of P3HT-ligated $CsPbBr_3$ ($D_{CsPbBr3}$ = 6, 8, and 10 nm; MW_{P3HT} = 5K, 10K, and 15K) via unimolecular, amphiphilic starlike block copolymer nanoreactors to effectively regulate their optical properties, and more importantly, charge separation dynamics at the P3HT/$CsPbBr_3$ QD interfaces, which have yet to be accessible by other approaches in the literature. Notably, placing semiconducting P3HT chains in intimate and permanent connection to $CsPbBr_3$ QDs extends the scope of the latter by yielding all semiconducting organic−inorganic nanomaterials with versatile structural complexity and functionalities over conventional small molecular organic ligand-capped perovskite QDs. Remarkably, as-crafted P3HT-ligated $CsPbBr_3$ QDs at the single-particle level display outstanding solubility in nonpolar organic solvent and long-term stabilities against high temperature, intense UV light irradiation, and polar solvents. In addition, DFT calculation substantiates the advantageous surface passivation of $CsPbBr_3$ QD with P3HT chains. In sharp contrast to the physical mixture of P3HT and $CsPbBr_3$ QDs, the intimate surface ligating of P3HT affords favorable type-II electronic band alignment with $CsPbBr_3$ QD, resulting in well-defined P3HT/$CsPbBr_3$ interfaces without phase segregation, more effective electronic interaction between them, and thus efficient charge carriers separation at the interfaces. More importantly, the interfacial charge separation efficiency is found to be influenced heavily by the MW of surface P3HT chains and diameter of $CsPbBr_3$ QDs due to MW-dependent charge carrier mobility of P3HT and size-related charge carriers transfer kinetics of $CsPbBr_3$ QDs, respectively. Taken the markedly enhanced stabilities and beneficial charge carrier separation together, such judiciously synthesized P3HT-ligated $CsPbBr_3$ could readily function as robust photocatalysts to render stable and controllable p-ATRP of a series of monomers, suggesting their enticing prospects for use in solar energy conversion. The reaction kinetics of p-ATRP are also seen to depend greatly on the MW of P3HT and the size of $CsPbBr_3$ QDs.

Conceptually, due to diverse CPs and precursors of perovskite QDs (or other semiconductors) that are amenable to the unimolecular starlike block copolymer nanoreactor strategy, an assortment of monodisperse, CP-ligated QDs with the desired band gap of each constituent and electronic band alignments between them can be conveniently accessed, thereby yielding peculiar electronic interaction and thus charge carriers dynamics in CP-ligated QDs. Due to the absence of phase segregation, incomplete surface coverage, or ambiguous surface chemistry of QDs widely encountered in conventional approaches (e.g., physically mixing, ligand exchange, or *in situ* synthesis of perovskite QDs with small-molecule ligands), the resulting uniform, CP-ligated QDs offer unique opportunity to elucidate the size- and surface chemistry-dependent photophysics of all semiconducting hybrid nanomaterials that underscore their potentials for use in optoelectronic devices, catalysis, sustainability, nanotechnology, etc.

ASSOCIATED CONTENT

Supporting Information

The Supporting Information is available free of charge at https://pubs.acs.org/doi/10.1021/jacs.2c04680.

Experimental details; schematic illustration of the p-ATRP process; and ^{1}H NMR, GPC, TEM, FT-IR, XRD, XPS, and optical characterization (Figures S1−S24 and Tables S1−S4) (PDF)

AUTHOR INFORMATION

Corresponding Author

Zhiqun Lin − *School of Materials Science and Engineering, Georgia Institute of Technology, Atlanta, Georgia 30332, United States;* orcid.org/0000-0003-3158-9340; Email: zhiqun.lin@mse.gatech.edu

Authors

Shuang Liang − *School of Materials Science and Engineering, Georgia Institute of Technology, Atlanta, Georgia 30332, United States; School of Chemical and Biomolecular Engineering, Georgia Institute of Technology, Atlanta, Georgia 30332, United States*

Sheng He − *Department of Chemistry, Emory University, Atlanta, Georgia 30322, United States*

Mingyue Zhang − *School of Materials Science and Engineering, Georgia Institute of Technology, Atlanta, Georgia 30332, United States*

Yan Yan − *School of Materials Science and Engineering, Georgia Institute of Technology, Atlanta, Georgia 30332, United States; School of Chemistry and Materials Science, Jiangsu Key Laboratory of Green Synthetic Chemistry for Functional Materials, Jiangsu Normal University, Xuzhou 221116, China*

Tao Jin − *Department of Chemistry, Emory University, Atlanta, Georgia 30322, United States*

Tianquan Lian − *Department of Chemistry, Emory University, Atlanta, Georgia 30322, United States;* orcid.org/0000-0002-8351-3690

Complete contact information is available at: https://pubs.acs.org/10.1021/jacs.2c04680

Notes

The authors declare no competing financial interest.

ACKNOWLEDGMENTS

This work was supported by the Air Force Office of Scientific Research (FA9550-19-1-0317). T.L. gratefully acknowledges the financial support from the National Science Foundation (CHE-2004080).

■ ADDITIONAL NOTES

[b] $M_{n,P3HT}$ is the MW of single-arm P3HT that is calculated based on ^{1}H NMR spectra following the below equation:

$$M_{n,P3HT} = \frac{A_a}{A_c} \times 168.30$$

where $M_{n,P3HT}$ is the MW of single-arm P3HT, A_a and A_c are the integral areas of thiophenyl protons on P3HT chain and alkynyl protons at the end of single chain, respectively, and 168.30 is the molecular weight of 3-hexylthiophene monomer.
[c] PDI of polymers was recorded by DMF GPC.
[d] The dimensions of $CsPbBr_3$ QDs were determined by performing image analysis on TEM images.

■ REFERENCES

(1) Protesescu, L.; Yakunin, S.; Bodnarchuk, M. I.; Krieg, F.; Caputo, R.; Hendon, C. H.; Yang, R. X.; Walsh, A.; Kovalenko, M. V. Nanocrystals of cesium lead halide perovskites ($CsPbX_3$, X = Cl, Br, and I): novel optoelectronic materials showing bright emission with wide color gamut. *Nano Lett.* **2015**, *15*, 3692−3696.

(2) Kim, Y.-H.; Kim, S.; Kakekhani, A.; Park, J.; Park, J.; Lee, Y.-H.; Xu, H.; Nagane, S.; Wexler, R. B.; Kim, D.-H.; et al. Comprehensive defect suppression in perovskite nanocrystals for high-efficiency light-emitting diodes. *Nat. Photonics* **2021**, *15*, 148−155.

(3) Swarnkar, A.; Marshall, A. R.; Sanehira, E. M.; Chernomordik, B. D.; Moore, D. T.; Christians, J. A.; Chakrabarti, T.; Luther, J. M. Quantum dot−induced phase stabilization of α-$CsPbI_3$ perovskite for high-efficiency photovoltaics. *Science* **2016**, *354*, 92−95.

(4) Shamsi, J.; Urban, A. S.; Imran, M.; De Trizio, L.; Manna, L. Metal halide perovskite nanocrystals: synthesis, post-synthesis modifications, and their optical properties. *Chem. Rev.* **2019**, *119*, 3296−3348.

(5) Zhu, X.; Lin, Y.; San Martin, J.; Sun, Y.; Zhu, D.; Yan, Y. Lead halide perovskites for photocatalytic organic synthesis. *Nat. Commun.* **2019**, *10*, No. 2843.

(6) Romani, L.; Speltini, A.; Ambrosio, F.; Mosconi, E.; Profumo, A.; Marelli, M.; Margadonna, S.; Milella, A.; Fracassi, F.; Listorti, A.; De Angelis, F.; Malavasi, L. Water-Stable $DMASnBr_3$ Lead-Free Perovskite for Effective Solar-Driven Photocatalysis. *Angew. Chem., Int. Ed.* **2021**, *60*, 3611−3618.

(7) Xu, Y.-F.; Yang, M.-Z.; Chen, B.-X.; Wang, X.-D.; Chen, H.-Y.; Kuang, D.-B.; Su, C.-Y. A CsPbBr3 perovskite quantum dot/graphene oxide composite for photocatalytic CO_2 reduction. *J. Am. Chem. Soc.* **2017**, *139*, 5660−5663.

(8) Kütahya, C.; Wang, P.; Li, S.; Liu, S.; Li, J.; Chen, Z.; Strehmel, B. Carbon Dots as a Promising Green Photocatalyst for Free Radical and ATRP-Based Radical Photopolymerization with Blue LEDs. *Angew. Chem., Int. Ed.* **2020**, *59*, 3166−3171.

(9) Huang, Y.; Zhu, Y.; Egap, E. Semiconductor quantum dots as photocatalysts for controlled light-mediated radical polymerization. *ACS Macro Lett.* **2018**, *7*, 184−189.

(10) Zhang, W.; He, J.; Lv, C.; Wang, Q.; Pang, X.; Matyjaszewski, K.; Pan, X. Atom Transfer Radical Polymerization Driven by Near-Infrared Light with Recyclable Upconversion Nanoparticles. *Macromolecules* **2020**, *53*, 4678−4684.

(11) Pan, X.; Tasdelen, M. A.; Laun, J.; Junkers, T.; Yagci, Y.; Matyjaszewski, K. Photomediated controlled radical polymerization. *Prog. Polym. Sci.* **2016**, *62*, 73−125.

(12) Fu, Y.; Zhu, H.; Chen, J.; Hautzinger, M. P.; Zhu, X.-Y.; Jin, S. Metal halide perovskite nanostructures for optoelectronic applications and the study of physical properties. *Nat. Rev. Mater.* **2019**, *4*, 169−188.

(13) Vickers, E. T.; Enlow, E. E.; Delmas, W. G.; DiBenedetto, A. C.; Chowdhury, A. H.; Bahrami, B.; Dreskin, B. W.; Graham, T. A.; Hernandez, I. N.; Carter, S. A.; et al. Enhancing Charge Carrier Delocalization in Perovskite Quantum Dot Solids with Energetically Aligned Conjugated Capping Ligands. *ACS Energy Lett.* **2020**, *5*, 817−825.

(14) Vickers, E. T.; Graham, T. A.; Chowdhury, A. H.; Bahrami, B.; Dreskin, B. W.; Lindley, S.; Naghadeh, S. B.; Qiao, Q.; Zhang, J. Z. Improving charge carrier delocalization in perovskite quantum dots by surface passivation with conductive aromatic ligands. *ACS Energy Lett.* **2018**, *3*, 2931−2939.

(15) Li, G.; Huang, J.; Li, Y.; Tang, J.; Jiang, Y. Highly bright and low turn-on voltage $CsPbBr_3$ quantum dot LEDs via conjugation molecular ligand exchange. *Nano Res.* **2019**, *12*, 109−114.

(16) Dai, J.; Xi, J.; Li, L.; Zhao, J.; Shi, Y.; Zhang, W.; Ran, C.; Jiao, B.; Hou, X.; Duan, X.; Wu, Z. Charge Transport between Coupling Colloidal Perovskite Quantum Dots Assisted by Functional Conjugated Ligands. *Angew. Chem., Int. Ed.* **2018**, *57*, 5754−5758.

(17) Xue, J.; Wang, R.; Chen, X.; Yao, C.; Jin, X.; Wang, K.-L.; Huang, W.; Huang, T.; Zhao, Y.; Zhai, Y.; et al. Reconfiguring the band-edge states of photovoltaic perovskites by conjugated organic cations. *Science* **2021**, *371*, 636−640.

(18) Gao, Y.; Shi, E.; Deng, S.; Shiring, S. B.; Snaider, J. M.; Liang, C.; Yuan, B.; Song, R.; Janke, S. M.; Liebman-Peláez, A.; et al. Molecular engineering of organic−inorganic hybrid perovskites quantum wells. *Nat. Chem.* **2019**, *11*, 1151−1157.

(19) Pang, X.; Zhao, L.; Han, W.; Xin, X.; Lin, Z. A general and robust strategy for the synthesis of nearly monodisperse colloidal nanocrystals. *Nat. Nanotechnol.* **2013**, *8*, 426−431.

(20) Roesing, M.; Howell, J.; Boucher, D. Solubility characteristics of poly(3-hexylthiophene). *J. Polym. Sci., Part B: Polym. Phys.* **2017**, *55*, 1075−1087.

(21) Westbrook, R. J. E.; Macdonald, T. J.; Xu, W.; Lanzetta, L.; Marin-Beloqui, J. M.; Clarke, T. M.; Haque, S. A. Lewis Base Passivation Mediates Charge Transfer at Perovskite Heterojunctions. *J. Am. Chem. Soc.* **2021**, *143*, 12230−12243.

(22) Yoon, Y. J.; Chang, Y.; Zhang, S.; Zhang, M.; Pan, S.; He, Y.; Lin, C. H.; Yu, S.; Chen, Y.; Wang, Z.; Ding, Y.; Jung, J.; Thadhani, N.; Tsukruk, V. V.; Kang, Z.; Lin, Z. Enabling Tailorable Optical Properties and Markedly Enhanced Stability of Perovskite Quantum Dots by Permanently Ligating with Polymer Hairs. *Adv. Mater.* **2019**, *31*, No. 1901602.

(23) Kim, J.; Lee, S.-H.; Lee, J. H.; Hong, K.-H. The role of intrinsic defects in methylammonium lead iodide perovskite. *J. Phys. Chem. Lett.* **2014**, *5*, 1312−1317.

(24) Hu, L.; Zhao, Q.; Huang, S.; Zheng, J.; Guan, X.; Patterson, R.; Kim, J.; Shi, L.; Lin, C.-H.; Lei, Q.; Chu, D.; Tao, W.; Cheong, S.; Tilley, R. D.; Ho-Baillie, A. W. Y.; Luther, J. M.; Yuan, J.; Wu, T. Flexible and efficient perovskite quantum dot solar cells via hybrid interfacial architecture. *Nat. Commun.* **2021**, *12*, No. 466.

(25) Harn, Y.-W.; Liang, S.; Liu, S.; Yan, Y.; Wang, Z.; Jiang, J.; Zhang, J.; Li, Q.; He, Y.; Li, Z.; Zhu, L.; Cheng, H.-P.; Lin, Z. Tailoring electrocatalytic activity of in situ crafted perovskite oxide nanocrystals via size and dopant control. *Proc. Natl. Acad. Sci. U.S.A.* **2021**, *118*, No. e2014086118.

(26) Ou, M.; Tu, W.; Yin, S.; Xing, W.; Wu, S.; Wang, H.; Wan, S.; Zhong, Q.; Xu, R. Amino-Assisted Anchoring of $CsPbBr_3$ Perovskite Quantum Dots on Porous g-C_3N_4 for Enhanced Photocatalytic CO_2 Reduction. *Angew. Chem., Int. Ed.* **2018**, *57*, 13570−13574.

(27) Miller, E. M.; Zhao, Y.; Mercado, C. C.; Saha, S. K.; Luther, J. M.; Zhu, K.; Stevanović, V.; Perkins, C. L.; van de Lagemaat, J. Substrate-controlled band positions in $CH_3NH_3PbI_3$ perovskite films. *Phys. Chem. Chem. Phys.* **2014**, *16*, 22122−22130.

(28) Liu, F.; Chen, D.; Wang, C.; Luo, K.; Gu, W.; Briseno, A. L.; Hsu, J. W.; Russell, T. P. Molecular weight dependence of the morphology in P3HT: PCBM solar cells. *ACS Appl. Mater. Interfaces* **2014**, *6*, 19876−19887.

(29) Perepichka, I. F.; Perepichka, D. F.; Meng, H.; Wudl, F. Light-Emitting Polythiophenes. *Adv. Mater.* **2005**, *17*, 2281−2305.

(30) Li, J.; Xu, L.; Wang, T.; Song, J.; Chen, J.; Xue, J.; Dong, Y.; Cai, B.; Shan, Q.; Han, B.; Zeng, H. 50-Fold EQE Improvement up to 6.27% of Solution-Processed All-Inorganic Perovskite $CsPbBr_3$

https://doi.org/10.1021/jacs.2c04680
J. Am. Chem. Soc. 2022, 144, 12901−12914

QLEDs via Surface Ligand Density Control. *Adv. Mater.* **2017**, *29*, No. 1603885.
(31) Zhao, L.; Pang, X.; Adhikary, R.; Petrich, J. W.; Lin, Z. Semiconductor Anisotropic Nanocomposites Obtained by Directly Coupling Conjugated Polymers with Quantum Rods. *Angew. Chem., Int. Ed.* **2011**, *50*, 3958−3962.
(32) Kobosko, S. M.; DuBose, J. T.; Kamat, P. V. Perovskite Photocatalysis. Methyl Viologen Induces Unusually Long-Lived Charge Carrier Separation in $CsPbBr_3$ Nanocrystals. *ACS Energy Lett.* **2020**, *5*, 221−223.
(33) Manser, J. S.; Kamat, P. V. Band filling with free charge carriers in organometal halide perovskites. *Nat. Photonics* **2014**, *8*, 737−743.
(34) Mocatta, D.; Cohen, G.; Schattner, J.; Millo, O.; Rabani, E.; Banin, U. Heavily doped semiconductor nanocrystal quantum dots. *Science* **2011**, *332*, 77−81.
(35) Schilinsky, P.; Asawapirom, U.; Scherf, U.; Biele, M.; Brabec, C. J. Influence of the molecular weight of poly (3-hexylthiophene) on the performance of bulk heterojunction solar cells. *Chem. Mater.* **2005**, *17*, 2175−2180.
(36) Krieg, F.; Sercel, P. C.; Burian, M.; Andrusiv, H.; Bodnarchuk, M. I.; Stöferle, T.; Mahrt, R. F.; Naumenko, D.; Amenitsch, H.; Rainò, G.; Kovalenko, M. V. Monodisperse long-chain sulfobetaine-capped $CsPbBr_3$ nanocrystals and their superfluorescent assemblies. *ACS Cent. Sci.* **2021**, *7*, 135−144.
(37) Shinde, A.; Gahlaut, R.; Mahamuni, S. Low-temperature photoluminescence studies of $CsPbBr_3$ quantum dots. *J. Phys. Chem. C* **2017**, *121*, 14872−14878.
(38) Shang, Q.; Kaledin, A. L.; Li, Q.; Lian, T. Size dependent charge separation and recombination in $CsPbI_3$ perovskite quantum dots. *J. Chem. Phys.* **2019**, *151*, No. 074705.
(39) Krys, P.; Matyjaszewski, K. Kinetics of atom transfer radical polymerization. *Eur. Polym. J.* **2017**, *89*, 482−523.
(40) Murray, C. B.; Norris, D. J.; Bawendi, M. G. Synthesis and characterization of nearly monodisperse CdE (E = sulfur, selenium, tellurium) semiconductor nanocrystallites. *J. Am. Chem. Soc.* **1993**, *115*, 8706−8715.
(41) Kalyuzhny, G.; Murray, R. W. Ligand Effects on Optical Properties of CdSe Nanocrystals. *J. Phys. Chem. B* **2005**, *109*, 7012−7021.
(42) He, S.; Li, Q.; Jin, T.; Lian, T. T. Contributions of exciton fine structure and hole trapping on the hole state filling effect in the transient absorption spectra of CdSe quantum dots. *J. Chem. Phys.* **2022**, *156*, No. 054704.
(43) Querner, C.; Reiss, P.; Sadki, S.; Zagorska, M.; Pron, A. Size and ligand effects on the electrochemical and spectroelectrochemical responses of CdSe nanocrystals. *Phys. Chem. Chem. Phys.* **2005**, *7*, 3204−3209.
(44) Pan, X.; Fang, C.; Fantin, M.; Malhotra, N.; So, W. Y.; Peteanu, L. A.; Isse, A. A.; Gennaro, A.; Liu, P.; Matyjaszewski, K. Mechanism of photoinduced metal-free atom transfer radical polymerization: experimental and computational studies. *J. Am. Chem. Soc.* **2016**, *138*, 2411−2425.
(45) Kütahya, C.; Schmitz, C.; Strehmel, V.; Yagci, Y.; Strehmel, B. Near-Infrared Sensitized Photoinduced Atom-Transfer Radical Polymerization (ATRP) with a Copper(II) Catalyst Concentration in the ppm Range. *Angew. Chem., Int. Ed.* **2018**, *57*, 7898−7902.

https://doi.org/10.1021/jacs.2c04680
J. Am. Chem. Soc. 2022, 144, 12901−12914